APPLIED SCIENCES AND ENGINEERING

Battery-free and AI-enabled multiplexed sensor patches for wound monitoring

Xin Ting Zheng[1]†, Zijie Yang[2,3]†, Laura Sutarlie[1], Moogaambikai Thangaveloo[4,5], Yong Yu[1], Nur Asinah Binte Mohamed Salleh[1], Jiah Shin Chin[4,6], Ze Xiong[3,7,8], David Lawrence Becker[4,5], Xian Jun Loh[1], Benjamin C. K. Tee[2,3,9,10]*, Xiaodi Su[1,11]*

Wound healing is a dynamic process with multiple phases. Rapid profiling and quantitative characterization of inflammation and infection remain challenging. We report a paper-like battery-free in situ AI-enabled multiplexed (PETAL) sensor for holistic wound assessment by leveraging deep learning algorithms. This sensor consists of a wax-printed paper panel with five colorimetric sensors for temperature, pH, trimethylamine, uric acid, and moisture. Sensor images captured by a mobile phone were analyzed by neural network–based machine learning algorithms to determine healing status. For ex situ detection via exudates collected from rat perturbed wounds and burn wounds, the PETAL sensor can classify healing versus nonhealing status with an accuracy as high as 97%. With the sensor patches attached on rat burn wound models, in situ monitoring of wound progression or severity is demonstrated. This PETAL sensor allows early warning of adverse events, which could trigger immediate clinical intervention to facilitate wound care management.

INTRODUCTION

Wound healing comprises of four stages, i.e., hemostasis, inflammation, proliferation, and remodeling (*1*). Impaired wound repair, such as chronic wounds and burn wound pathological scars, is often stalled in the proinflammatory phase and presents a major health and economic burden worldwide (*2*, *3*). Now, wound healing is typically examined visually by clinicians (*4*). Wound infections are mostly diagnosed via "swabbing" followed by a bacteria culture with long turnover times, which does not provide timely wound diagnosis (*5*, *6*). In addition, quantitative measurements of biochemical markers are generally limited to laboratory testing, such as enzyme-linked immunosorbent assays. In general, current wound monitoring methods are slow and lack of holistic profiling and quantitative characterization for wound healing status, making accurate prediction of wound healing trajectory difficult in hospitals (*7*). In addition, current wound assessment typically requires frequent manual removal of dressing, which elevates risks of infection and may cause additional trauma.

Thus, wearable wound sensor patches have been proposed to tackle the above challenges faced in wound monitoring (*2*). Current reported wound sensors have largely focused on detecting a single physical or biochemical marker, such as temperature (*8*), pH (*9*), uric acid (UA) (*10*), or pathogenic bacteria–related deoxyribonuclease (*11*), mostly relying on electrochemical sensors. For example, Kalasin *et al.* (*12*) developed a deep artificial neural network to monitor pH via pH-responsive voltage output and for healing stage recognition with high accuracy. However, it is only for a single parameter, and it still required an energy source on the devices (*13*).

The emergence of flexible electronics has enabled different sensors to be integrated into a single platform while providing conformational contact with the human skin (*14*–*19*). This has paved the way for wearable biosensors that can detect dual or even multiple biomedical parameters of the wound environment (*10*, *20*–*22*). For example, an array of flexible potentiometric pH sensors and a flexible thermometer were successfully embedded into a smart bandage to assess the wound status every minute for up to 20 hours (*23*). A flexible electronic biosensing platform with integrated microfluidic wound exudate collector was reported for profiling of three wound inflammation mediators, microbial burden, temperature, and pH with a smartphone-based wireless data collection every minute for typically 1-hour duration (*24*). However, the abovementioned electrochemical sensors required bulky printed circuit boards and batteries. They were also affected by motion artefacts and required frequent calibrations.

Although electrochemical/electrical sensors can offer fast and real-time monitoring by the sophisticated electronic sensors that collect and display data every second or every minute (*25*), such advantages are not essential for wound healing monitoring, because the wound healing process is much longer over many days. Optical detection techniques, such as wax-printed paper fluidic colorimetric and fluorometric sensors (*26*–*28*), are promising point-

[1]Institute of Materials Research and Engineering (IMRE), Agency for Science Technology and Research (A*STAR), 2 Fusionopolis Way, Innovis #08-03, Singapore 138634, Republic of Singapore. [2]Department of Materials Science and Engineering, National University of Singapore, 9 Engineering Drive 1, Singapore 117576, Republic of Singapore. [3]Institute for Health Innovation and Technology (iHealthtech), National University of Singapore, MD6, 14 Medical Drive, Singapore 117599, Republic of Singapore. [4]Lee Kong Chian School of Medicine, Nanyang Technological University, 11 Mandalay Road, Singapore 308232, Republic of Singapore. [5]Skin Research Institute of Singapore (SRIS), Agency for Science Technology and Research (A*STAR), 11 Mandalay Road, Singapore 308232, Republic of Singapore. [6]A*Star Skin Research Laboratory (ASRL), Agency for Science Technology and Research (A*STAR), 11 Mandalay Road, Singapore 308232, Republic of Singapore. [7]Department of Biomedical Engineering, National University of Singapore, Singapore 117576, Republic of Singapore. [8]Wireless and Smart Bioelectronics Lab, School of Biomedical Engineering, ShanghaiTech University, Shanghai 201210, China. [9]The N.1 Institute for Health, National University of Singapore, 28 Medical Drive. #05-COR, Singapore 117456, Republic of Singapore. [10]Department of Electrical and Computer Engineering, National University of Singapore, Block E4, 4 Engineering Drive 3, Singapore 117583, Republic of Singapore. [11]Department of Chemistry, National University of Singapore, Block S8, level 3, 3 Science Drive 3, Singapore 117543, Republic of Singapore.
*Corresponding author. Email: benjamin.tee@nus.edu.sg (B.C.K.T.); xd-su@imre.a-star.edu.sg (X.S.)
†These authors contributed equally to this work.

of-care diagnostics devices, which could be alternatives for in situ wound monitoring. For wound monitoring, existing optical sensors, for example, a hydrogel dressing with a fluorescent glucose sensor and a colorimetric pH sensor embedded, have been demonstrated to simultaneously detect both parameters in the wound environment (*29*). However, it can measure only two analytes and required specialized equipment to measure the analytes.

Here, we report a paper-like battery-free in situ AI (artificial intelligence)–enabled multiplexed (denoted as PETAL) sensor patch for holistic wound healing monitoring. Five colorimetric sensors for temperature, pH, trimethylamine (TMA), UA, and moisture, exploiting different sensing principles and materials, are integrated into a single piece of paper sensor patch. The sensor patch allows quantitative characterization of each biomarker within minutes (for each test). The PETAL sensor patch detects carefully selected biomarkers related to wound inflammation, infection, and wound environment condition. It is flexible and thus feasible to be integrated with wound dressings for in situ analysis without needing to remove the wound dressing.

Using a deep learning–based AI algorithm, our sensor patch simply requires a modern smartphone to provide a holistic assessment of the wound healing status, enabling the classification of wound types/severity levels. We demonstrate the assessment of wound status for chronic wounds or burn wounds both ex situ (via the wound exudate) and on rat models (direct adhesion of the sensor patches). Such wearable multiplexed sensors coupled with AI analytics are envisioned to allow early warning of adverse events and thus trigger immediate clinical intervention. Providing earlier access of wound healing status to clinicians with less interruption to the wound has the potential to expand sophisticated wound care management in various health care settings including homes (*30*).

RESULTS

Design and fabrication of the paper fluidic–based wound sensor patch

Figure 1 shows the paper fluidic wound sensor patch that can be applied onto a burn wound or a chronic wound for holistic assessment. A double-sided wax-printed paper fluidic panel has channels to the sensing regions on the upper side with a circular inlet at the skin interface. This paper panel is then sandwiched between a top transparent silicone layer and a bottom adhesive wound contact layer, also having a circular center opening (Fig. 1A).

The surface transparent layer allows for normal skin functions of oxygen and moisture exchange while allowing image display for accurate image capture and analysis. The bottom wound contact layer protects the wound bed from direct contact with the sensor panel to minimize wound tissue disruptions. This bottom layer is also adhesive to skin for gentle attachment of sensor patch (Fig. 1A). In between the paper sensor panel and the bottom adhesive contact layer is a blood filtration membrane, i.e., Whatman blood filtration membrane (LF1 grade), which shows complete removal of red blood cells from wound exudate (fig. S1). When the assembled PETAL patch is put on a wound, the wound exudate will come into contact with the blood filtration membrane first and pass through the filtration membrane to lastly reach the paper sensor panel. As wound exudate flows into the paper sensor panel through the back center port, the respective sensors at the five detection zones will change color according to respective analyte concentration.

This sensor patch is light, thin, and flexible and can stand up against a Pinwheel flower (Fig. 1, B and C). The fluidic pattern resembles the five-petaled Pinwheel flower, so we call this sensor patch PETAL. Such a flexible, low-cost, and battery-free sensor patch is potentially suitable for integration with wound dressings. Figure 1D illustrates the model of the machine learning algorithm used in this work for wound classification.

The key considerations of the wax-printed paper fluidic panel include the choice of cellulose paper, the arrangement of the five sensing regions in connection to sampling channel, and the wax pattern–related optimization (dimensions, geometry, printing parameters, etc.).

Cellulose paper of 6 μm pore size and 390 μm thickness was selected in this study because of their good molecular retention property. The five detection zones on the upper surface of the paper panel for loading the sensing materials are arranged in a five petaled-flower like pattern, connected by five channels through a center opening at the bottom surface, from where wound exudate can flow in, resembling a five-petaled flower (Fig. 1B). Such an arrangement allows equal channeling of wound exudates to the detection zones.

The outer dimensions of the sensor panel (in centimeter scale) as well as its channel width and detection zone diameter can be tailored to suit the actual wound size as well as the amount and viscosity of wound exudate. Figure S2 shows three different sized sensor patches (1.8-, 2.5-, and 3.5-cm squares) that we have printed, and the volumes needed for a simulated wound fluid (SWF) of a low viscosity (~1 mPa·s) and a SWF of a high viscosity (~ 80 mPa·s) added with 0.5 weight % (wt %) xanthan gum. The smallest patch tested so far has a size of 1.8 cm. It is also possible to place multiple small-sized sensor patches over a large wound area to collect spatial information in the future.

After the sensor panel was printed with the respective wax patterns on both sides, it was heated up briefly to 90°C to melt the wax so that it can penetrate the cellulose matrix to form a continuous barrier, upon cooling down, to define the paper fluidic pattern. On the other hand, overheating will narrow the fluidic channel. As wound exudate is viscous with abundant metabolites and proteins, it easily clogs up the channels if the channels become too narrow/shallow. Therefore, we have optimized the heating time (10 min) to ensure a quick and smooth flow of SWFs in the wax-printed channels to reach the detection zones in 2 to 3 min (fig. S3).

Colorimetric sensor development and calibration

Five colorimetric sensors were prepared for inflammation, infection, and wound environment indicators, including temperature, pH, moisture, TMA, and UA. Tables S1 and S2 show the clinical significance of the five selected biomarkers in chronic wounds and burn wounds. In particular, the increase in chronic wound temperature indicates infection and delayed healing (*30*, *31*). Similarly, burn wounds increase their temperature to maintain hypermetabolic process leading to hyperthermia (*32*). Normal skin pH is slightly acidic, and pH is usually elevated to alkaline range in nonhealing wounds including both chronic wounds and more severe burn wounds (*29*, *33*, *34*). Wound moisture level is critical to healing, but it varies substantially with the type of wound dressing. Therefore, moisture readings were only used as reference in this work to

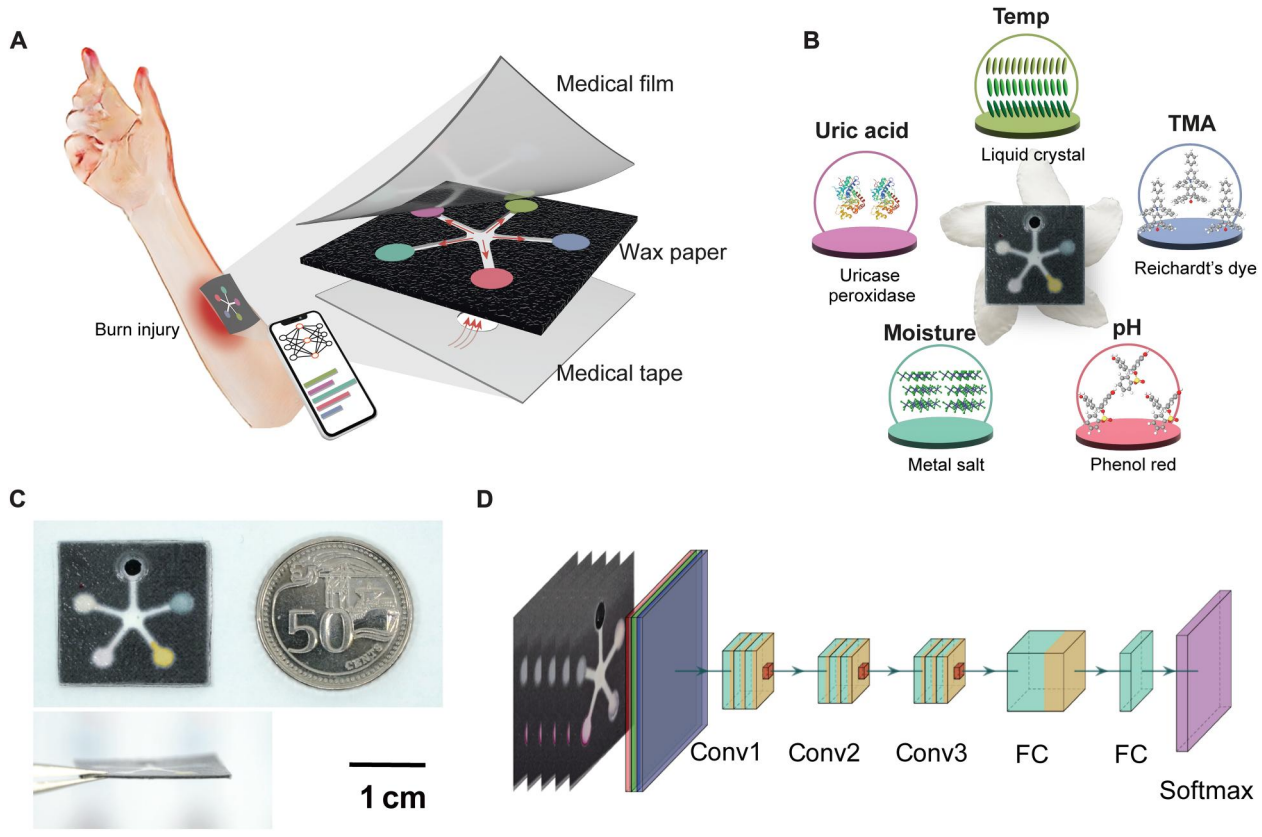

Fig. 1. Schematic of a battery-free colorimetric multiplexed sensor for wound monitoring. (**A**) Illustration of the PETAL sensor adhered onto a burn wound for colorimetric analysis of wound healing status with the detailed layer-by-layer structure of the PETAL sensor. (**B**) The real sensor patch, resembling a five-petaled Pinwheel Flower (*Tabernaemontana divaricata*), and the sensing materials/principles for each colorimetric sensor. (**C**) The real sensor patch and its side view, next to a 50 cent Singapore coin. (**D**) Neural network–based machine learning algorithm for wound classification, its architecture includes multiple convolutional layers (Conv), two fully connected layers (FC) and a softmax layer.

indicate sufficient channeling of wound exudate to the detection zones and successful activation of colorimetric sensors (*4*, *35*). TMA is a volatile organic compound (VOC) produced by many wound bacteria such as *Pseudomonas aeruginosa*, and a high TMA level [>30 parts per million (ppm)] detected at wound sites strongly indicates wound infection (*36*, *37*). UA is the end product from the purine catabolic pathway, and an elevated UA level suggests prolonged inflammation and has been correlated with wound severity in burns. On the other hand, decreased UA levels are related to bacterial colonization (*10*, *25*, *38*, *39*). These markers/parameters together provide a holistic profiling and quantitative characterization of wound infection status and the wound healing process.

In this study, the five colorimetric sensors used different sensing materials [cholesteric liquid crystals (CLCs) for temperature, organic dyes for pH and TMA, metal ions for moisture, and enzymes for UA] with customized formulations, involving polymer matrix, stabilizer, additives, etc. To achieve the desired limit of detection and clinically relevant dynamic range, sensor preparation processes were also customized, including paper surface treatment, sensing material loading amount, and dying conditions. For the five sensors to coexist with good sensing performances on the same sensor panel, they were prepared sequentially in the five detection zones. Detailed sensor preparations are described below in the order of sensor preparation (Fig. 2A).

First, the temperature sensor was prepared using CLCs, whereby the rotation and orientation of the liquid crystal molecules change with the change in temperature. A typical CLC temperature sensor suits normal skin temperature in the range of 31° to 35°C and with persistent 1°C increase relative to normal baseline level indicating infection/nonhealing state (*30*, *31*). In this study, a three-component mixture of cholesterol derivatives—cholesteryl oleyl carbonate (COC), cholesteryl benzoate (CB), and cholesteryl nonanoate (CN)—was used. Varying the composition of CLC mixture gives a different color gradient and a different temperature range (fig. S4). To achieve temperature sensing range of 31° to 36°C on cellulose paper substrate, the CLC mixture was optimized to 36% COC, 10% CB, and 54% CN, which displays distinct color changes gradually from red to green to blue as temperature increased from 31° to 36°C, with a linear change in the intensity ratio (i.e., the ratio of reflectance at 418 nm over the sum of reflectance at 520 and 650 nm) in the dynamic range (Fig. 2B). A high ambient temperature (i.e., the temperature of the air) may possibly affect the wound surface temperature. However, as the thermal conductivity of a solid is greater than that of the air, the CLC temperature sensor would be more sensitive to the temperature of the solid surface, i.e., the

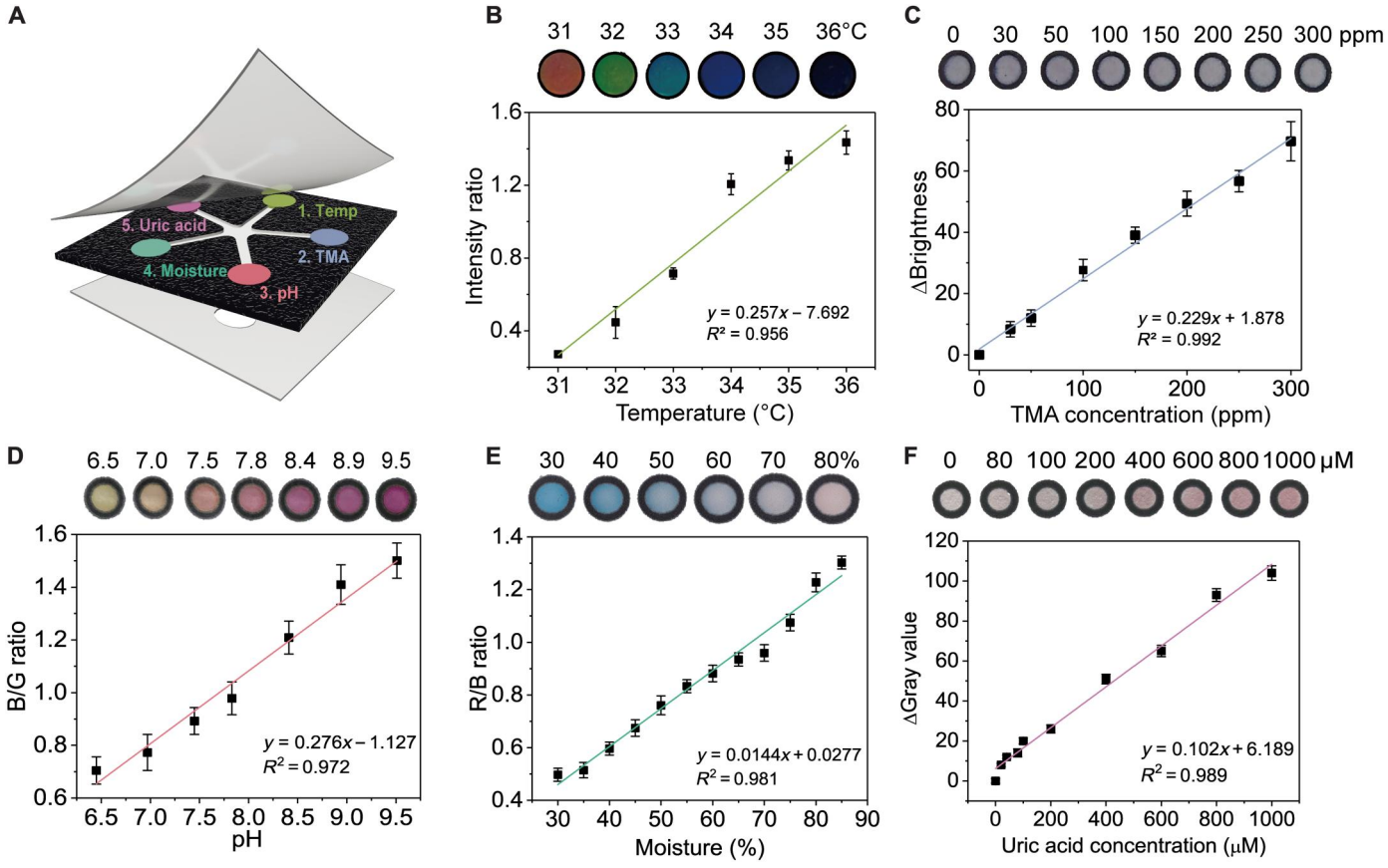

Fig. 2. Characterization of the colorimetric sensors. (**A**) Detailed layout of the five sensors in the wax-printed sensor panel. Calibrations of (**B**) temperature sensor, (**C**) TMA sensor, (**D**) pH sensor, (**E**) moisture sensor, and (**F**) UA sensor. All error bars in (B) to (F) represent the SD from three sensors.

wounded skin for this study, where the sensor is attached on. Our experiment confirmed this notion as shown by fig. S5.

Second, the TMA sensor was prepared using Reichardt's dye, a solvatochromic dye that changes color based on molecular polarity (*40*, *41*). This dye gives specific color change from dark gray to light white upon detection of TMA as the molecular structure and polarity of TMA (a tertiary amine) are unique and different from other common molecules in wound exudate (e.g., proteins, UA, and salt). To intensify the color response to TMA on the sensor panel, the cellulose paper matrix in the second detection zone was treated with perfluorooctyltrimethoxysilane before loading the Reichardt's dye, and a high contrast color change by TMA was then observed (fig. S6). We postulate that the TMA molecules interact better with the Reichardt's dye on the hydrophobic paper or that the perfluorooctyltrimethyoxysilane induces the initial polarity of the environment where the Reichardt's dye is placed so that additional polarity change by TMA results in a more distinct color change. The responses of the optimized Reichardt's dye on the silane-treated paper to various TMA concentrations are shown in Fig. 2C. The color change from gray to bright was analyzed on the basis of the change of brightness value that covers the wound relevant range of 30 to 300 ppm (*37*).

Third, the pH sensor was based on phenol red dye due to its biocompatibility and its pK_a (where K_a is the acid dissociation constant) of 7.9, rendering it suitable for detecting wound pH as shown in table S1. When the pH is below 6.8, phenol red is present in the form of monovalent ions and appears yellow. When the pH is above 8.2, phenol red further deprotonates to a divalent ion and appears magenta (fig. S7). As shown in Fig. 2D, the blue-to-green (B/G) ratio correlated with the solution pH well with a dynamic range of pH 6 to 10 and a resolution of ~0.5 pH.

Fourth, a moisture sensor is based on anhydrous cobalt chloride impregnated in the polyvinyl alcohol (PVA) matrix in the detection zone, which chelates with water molecules to form a hexahydrate cobalt chloride that displays a color change (*42*). As the moisture content increased, the color of the moisture sensor changed from deep blue to pale violet to pink, and the red-to-blue (R/B) ratio showed a good correlation with the moisture level (Fig. 2E).

In the fifth detection zone, a colorimetric UA sensor was developed on the basis of a cascade enzymatic reaction using both uricase and peroxidase (*43*). In the first step, uricase catalyzes UA conversion and generates H_2O_2 as a by-product. In the second step, horseradish peroxidase (HRP) converts the chromogenic substrate [such as the 4-aminoantipyrine (4-AAP)] to a dark pink–colored product in the presence of as-formed H_2O_2 (fig. S8). Many colorimetric paper strips are reported for one-time immediate use (*44*). In the case of wound monitoring, however, the wound healing process may take days and even weeks. Thus, for continuous in situ wound monitoring, the enzymatic sensor must achieve the following criteria: (i) good color stability for tracking color change over

tens of hours, (ii) well-maintained enzyme activity in the wound environment, (iii) good retention of colorimetric sensing reagents, (iv) similar calibration performance in phosphate-buffered saline (PBS) buffer versus SWF, and (v) no false-positive signals. To achieve these goals, we optimized the UA sensor by carefully tuning the polymeric matrix pH, the enzyme dissolution medium, filter paper type, and the chromogenic substrate to achieve good color stability and well-maintained enzyme activity for wound status analysis (fig. S9). A linear calibration using a change in gray value (ΔGray value) was established for a dynamic range of 40 to 1000 μM with a detection limit of 40 μM, which covered the clinically relevant UA concentration range in wounds well (Fig. 2F). We then verified that the detections of the five markers do not interfere with each other in PBS buffer when they are assembled on a single patch (fig. S10).

Quantitative analysis of SWFs with the PETAL sensor patch

To demonstrate that our PETAL sensor patch can simultaneously analyze five wound biomarkers/indicators, we first composed two SWFs (*45*). SWF-A has no TMA added but high UA concentration (600 μM) to simulate a normal healing wound (*46*), while SWF-B contains a high TMA level (300 ppm) but a very low UA concentration (60 μM) to represent an infected nonhealing wound (*37*) without any pH adjustments. The images of the wax-printed sensor patches before SWF addition were used as the baseline for color analysis (Fig. 3A), and a time-lapse image series were captured upon the addition of SWF-A at 31°C and SWF-B at 32°C (Fig. 3A) to the back center port. It takes around 3 min for SWF to flow to the edge of the detection zones upon addition from the center port, and all sensors are fully filled with SWF at 8 min (fig. S11). We have set 15 min upon the SWF addition as the standard time for image taking, which is sufficient for all sensors being fully reacted to generate stable color change. The differences between SWF-A and SWF-B are qualitatively compared in Fig. 3B. Through color analysis, the sensor patches clearly differentiate the two SWFs representing different wound conditions (Fig. 3, D to H).

In the first detection zone, the temperature sensor changes color from red to green. The intensity ratio also increases above the threshold of 0.45, indicating that the increase in temperature is greater than 1°C, which is reflective of the higher temperature operated mimicking the infection condition. In the second detection zone, the TMA sensor retains its original dark gray color when exposed to healing SWF-A, but the color almost completely bleached upon SWF-B addition. Meanwhile, the change in brightness (ΔBrightness) increases above the dashed line (representing the TMA threshold level of 30 ppm for bacterial infection) confirmed the presence of abundant TMA in this infected SWF-B. In the third detection zone, the colors of the pH sensors for the two SWFs are similar as compared to the initial patch, all showing yellow to orange colors because pH values of these two SWFs are not artificially adjusted and stay within the neutral range (around pH 7.0 to 7.5).

In the fourth detection zone, more than 4 μl of SWF was needed to activate the moisture sensor with R/B ratio starting to increase above the baseline fluctuation of ~0.6 (fig. S12). At above 7 μl, the

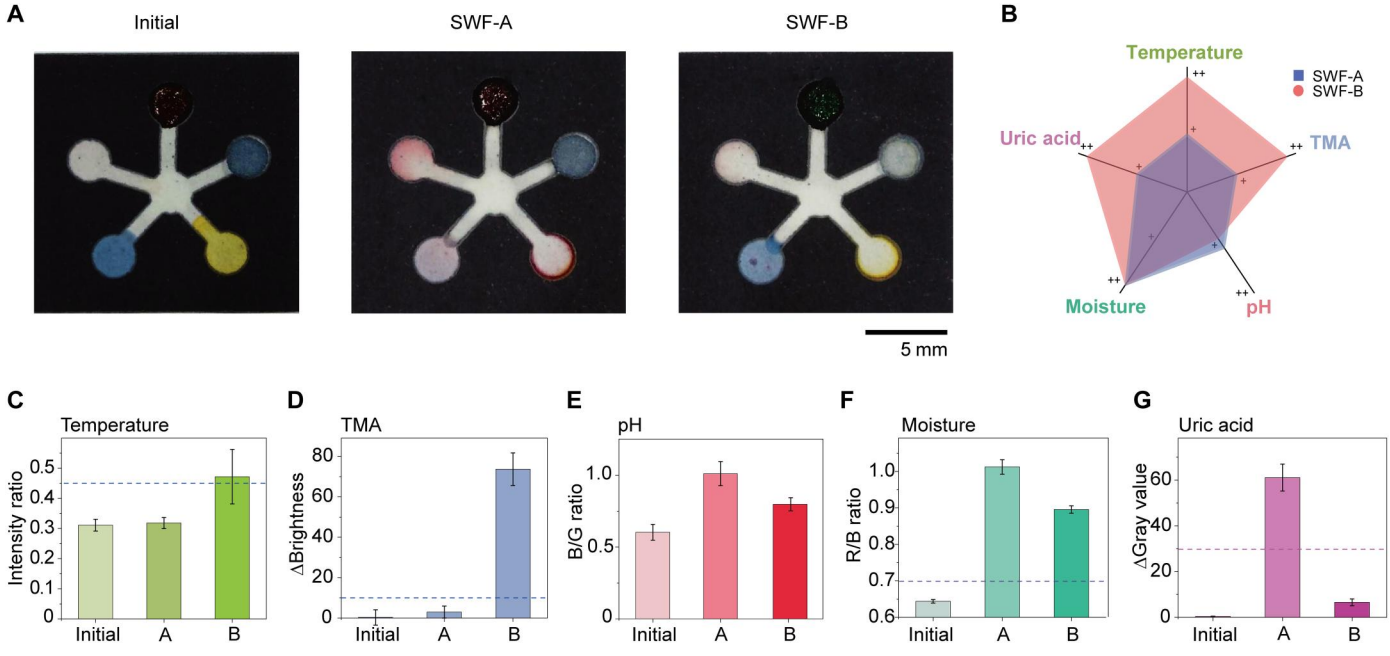

Fig. 3. Quantitative analysis of sensor patch responses to SWFs. (**A**) Photos of the sensor patches before and after exposure to two types of SWFs. (**B**) Radial graph showing the different levels of the five markers in SWF-A and SWF-B. (**C** to **G**) Color analysis for the five parameters, respectively. The dashed line in each of the bar figures is the cutoff values differentiating condition A versus B. (C) Intensity ratio increases above the dashed line means the change in temperature is greater than 1°C, indicating wound infection. (D) ΔBrightness increases above the dashed line indicate sufficient TMA formation above 300 ppm and wound infection. (E) The pH sensor indicates the pH values of both SWFs are in the neutral range when compared to calibration line in Fig. 2. (F) The R/B ratio rises above the baseline fluctuation of 0.6 as SWF enters the fourth detection. A value of 0.7 is selected as the threshold to indicate that the moisture level has reached ~50% and sufficient exudate has reached the patch. (G) ΔGray value drops below the dashed line, meaning that the UA concentration has decreased at least 50% with respect to SWF-A, indicating possible prolonged inflammation or wound infection. All error bars in (C) to (G) represent the SD from three replicates.

moisture sensor turned totally into pink color (R/B ratio > 1), showing that the detection zone has been fully filled up. This moisture sensor acts as a reference to assure that sufficient exudate has reached the detection zones. Last, in the fifth detection zone, the initially colorless UA sensor turns into an intense pink color for SWF-A, while it shows a light pink color for SWF-B. For SWF-B, ΔGray value drops below the dashed line, which means that the UA concentration has decreased at least 50% with respect to the SWF-A, confirming the lower UA present in this wound fluid mimicking prolonged wound inflammation or infection. With this benchtop experiment, we successfully demonstrated the prominent color responses for all five sensors in the PETAL sensor and no interference between the different sensors. Quantitative color analysis of the sensor patches reveals distinct differences for two different SWFs, hinting its capacity for accurate determination of wound status.

Paper-based microfluidic devices typically experience corona effect (also known as coffee-ring phenomenon), which is related to the flow patterns, evaporation physics, and deposition structures after solvent evaporation (*47*, *48*). We observed strong corona effects for pH sensor and mild corona effects for moisture and UA sensors, but not for temperature and TMA sensors. To minimize the impact of corona effect on the calibration accuracy, we measured the intensity or RGB value of the entire circular region of the detection zones as defined by the black boundaries. Using pH sensor as an example, we have compared its calibrations from the sensor zones with different degrees of corona effects (fig. S13) and confirmed the consistency of the B/G ratios (<3% difference), regardless the spatial distribution of the color.

To study the amount of liquid that the PETAL patch can take up and the potential impact of high fluid amount on the color retention in the detection zones, we tested up to ~30 μl of SWF, which exceeded the volume of 8 μl needed to saturate the detection zones and the volume of 20 μl that the liquid will overflow. We found no color leaching or reagents backflowing toward the channels (fig. S14) with such a high volume of liquid. As for the storage stability, all the sensors except UA sensor are stable (i.e., the reagents remain active) for at least 3 months. For the enzyme-based UA sensor, it retains >80% activity for 1 week stored at room temperature in a normal plastic sealed bag (fig. S15). The series of time-lapse images (one frame per 15 s) showing the change of color over 15 min were subsequently used as the training dataset to develop the machine learning algorithm for wound classification with SWF-A representing normal state and SWF-B representing the perturbed state.

AI analysis of PETAL sensor patch upon exposure to animal wound exudates

To demonstrate that our PETAL sensor patch can be used directly to analyze real wound exudates, we tested our sensor patches with two kinds of animal wound exudates from rat models, i.e., perturbed wound exudate from rats, which mimics a nonhealing chronic wound, and burn wound exudate from rats. To create a perturbed wound model, a full thickness excisional wound was first created in rat with a 6-mm biopsy punch. A scaffold impregnated with a senescence inducing agent was then inserted into the wound and left in situ for 10 days to generate the perturbed wounds (Fig. 4A). Perturbed wounds display obvious swollen wound edges, a red ring of inflammation, altered biomolecular expression, and delayed wound closure, which nicely mimic features of human chronic wounds (*49*). We compared the perturbed wound exudate collected on day 10, and the elution from the scaffold that has been placed in the wound for 10 days.

As shown in Fig. 4B, distinct color differences for the pH sensor and the UA sensor can be visually detected upon the addition of the 10th day exudate and scaffold elution. Referring to the sensor calibration curves (Fig. 2), the perturbed wound exudate shows a more alkaline pH of 9.2 as compared to the scaffold fluid with pH 7.8 (Fig. 4D). Note that the UA level in the 10th day wound exudate is only ~300 μM, which is more than twofold lower compared to the fluid eluted from the scaffold (Fig. 4C). It is postulated that the scaffold, left in the wound for 10 days, will have absorbed wound exudate from days 1 to 10. The wound exudate collected on day 10 specifically represents the wound condition on scaffold removal, which is already in the nonhealing state. The pH for exudate following scaffold removal is more alkaline (nonhealing indication), while the pH of the scaffold fluid is closer to neutral range but still above the normal skin pH of 5.6. This also explains why the accumulated scaffold fluid contains much higher UA, while the 10th day wound exudate shows lower UA, indicating nonhealing perturbed wound. After feeding to our neural network #1, the model gives a high accuracy of 96.3% in determining the normal state versus the perturbed state (Fig. 4D), which suggests the feasibility for identification of chronic wounds with pretrained convolutional neural network (CNN) (figs. S16 to S18).

For burn wound types, partial thickness burn extends from epidermis downward deep into the reticular dermis or into the deeper layers of dermis. Depending on the extent of the burn, the vasculature may or may not be present and could be sluggish when pressure is applied (*50*). The partial burns are simulating second degree burns that typically require surgery and form more scars but are less painful than deep burns. The deep burns represent the full thickness third degree burns that have a high risk of infection and require skin grafting. The depth of the deep burn extends through the epidermis and all layers of dermis and into subcutaneous layer. The vascular permeability in the deep burn is compromised and leads to tissue edema and along with hypercoagulability and vessel thrombosis that could further impair dermal perfusion (*51*). Moreover, burn progression often also occurs in the presence of increased release of cytokines, inflammatory response, and oxidative stress into the extracellular space (*52*). As described by the Jackson′s burn model, the initial zone of stasis can convert into zone of coagulation if dermal vascular network is not restored and intervention is not optimal (*53*). A sensor that measures a specific wound biomarker is useful to identify the state of the wound and cater to optimal treatment.

In this study, 55° and 85°C (10 s of burn creation) were used to create representative partial burn and deep burn wounds, respectively (Fig. 5A). As the days passed, wound exudate collection became more challenging for deep burns, as the deep burn turned necrotic and lost the blood restoration functionality. Wound exudate samples were collected from the partial thickness burns and deep burns from post-burn day (PBD) 1 to PBD 3. The day of burn creation was labeled as day 0, and PBD 1 refers to 24 hours after burn creation. We were able to collect substantial amounts of wound exudate per rat (>100 μl for the four 6-mm burns per rat) overnight under the Tegaderm wrapping. This exudate volume agrees well with the burn wound exudate production rate of 0.34 to 0.43 g/cm^2 per 24 hours (equals to 4 to 5 μl/hour

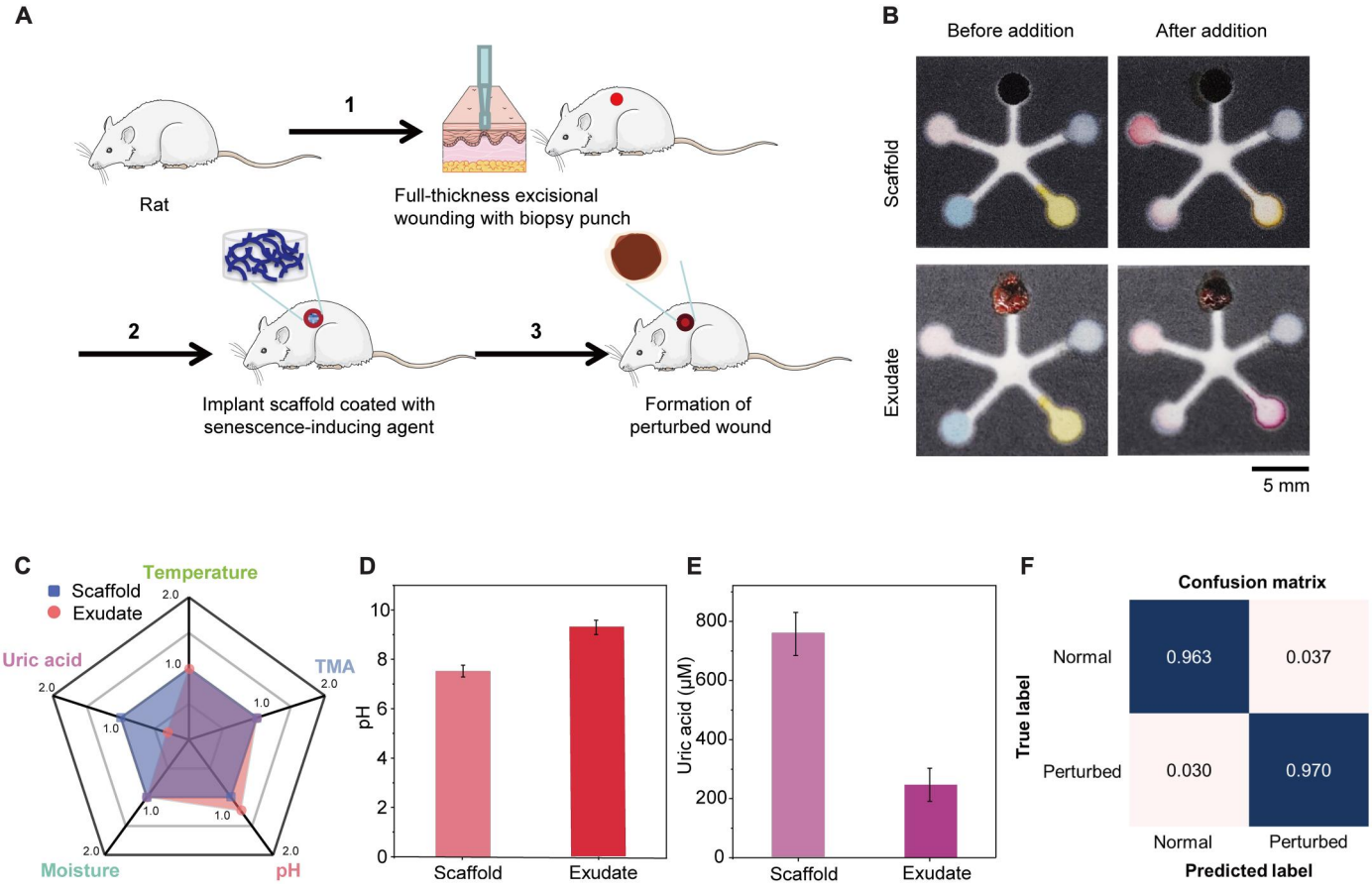

Fig. 4. Ex situ benchtop analysis of perturbed wound exudate. (**A**) The formation of perturbed wounds. (**B**) Sensor images before and after addition of perturbed wound exudate versus extracted fluid from scaffold. (**C**) Radial graph giving an overview scale of the five markers in the perturbed wound exudate versus the scaffold extract. Quantitative comparisons of (**D**) pH levels and (**E**) UA concentrations. Error bars in (D) and (E) represent the SD (n = 3). (**F**) Confusion matrix for perturbed wound model.

for the 6-mm burn wound in our experiments) (*54*). It was more than sufficient for ex situ measurements using our sensor patch (the 1.8-cm square), which only requires ~8 μl (fig. S2C).

The exudate samples were kept frozen until used to test the PETAL sensor patches, in comparison with the initial sensor patch before exudate addition (Fig. 5B). For benchtop testing, the wound exudate temperature has been set to 32° to 33°C. The temperature sensor reflects this range that displays green to blue color. For the TMA sensor, no change in the initial blue gray color was observed, indicating that TMA was not detected. This agreed with the fact that the rats were kept in sterile animal facilities, and there was no infection. On PBD 1, the pH values for both the partial and deep burns were around 7.5, which increased slightly to ~8 on PBD 2 and then reduced again on PBD 3 toward near neutral value but were still above the pH 5.6 of normal skin (Fig. 5C).

For UA, the trend differs substantially for the partial versus deep burns. In the partial thickness burns, the UA concentration remained almost constant at ~40 μM over 3 days. For the deep burns, the UA level was similar to that of partial thickness burns at ~40 μM on PBD 1, but it sharply increased about fivefold to ~180 μM on PBD 2 and then dropped to ~120 μM on PBD 3 (Fig. 5D). The moisture sensor turned pink when the exudate was initially added and reverted to a blue color when the exudate dried up at the end of detection. When we plotted the fold change of the five markers/indicators on radial charts, it is obvious that only UA shows a sharp change over 3 days, while the other markers/indicators show minimal change, which further suggests UA as the most critical marker to distinguish partial thickness versus deep burns in their biochemical profiles (Fig. 5, F to H). Our neural network model #2 achieves a high accuracy of 92.6% with very low training loss for identification of partial thickness burns versus deep burns (Fig. 5E and figs. S16 and S17).

In situ burn wound severity analysis in rat models

To demonstrate the applicability of the PETAL sensor patch for in situ wound monitoring, we performed longitudinal wound monitoring in the rat burn wound models for 4 days (Fig. 6, A and B) with the sensor patches attached to the wound sites. Briefly, on each rat, two partial thickness burns at 55°C and two deep burns at 85°C were induced on the back of the rats on day 0. One of the partial or deep burns was used as control with the other having a PETAL sensor patch adhered on top (Fig. 6C) to assess the biocompatibility of sensor patches. The sensor placements on the four burn wounds were systematically varied in rat 1, rat 2, and rat 3 (fig. S19). Subjects were allowed to move freely with the attached sensor patches for 6 hours, and images of the sensor patches were taken

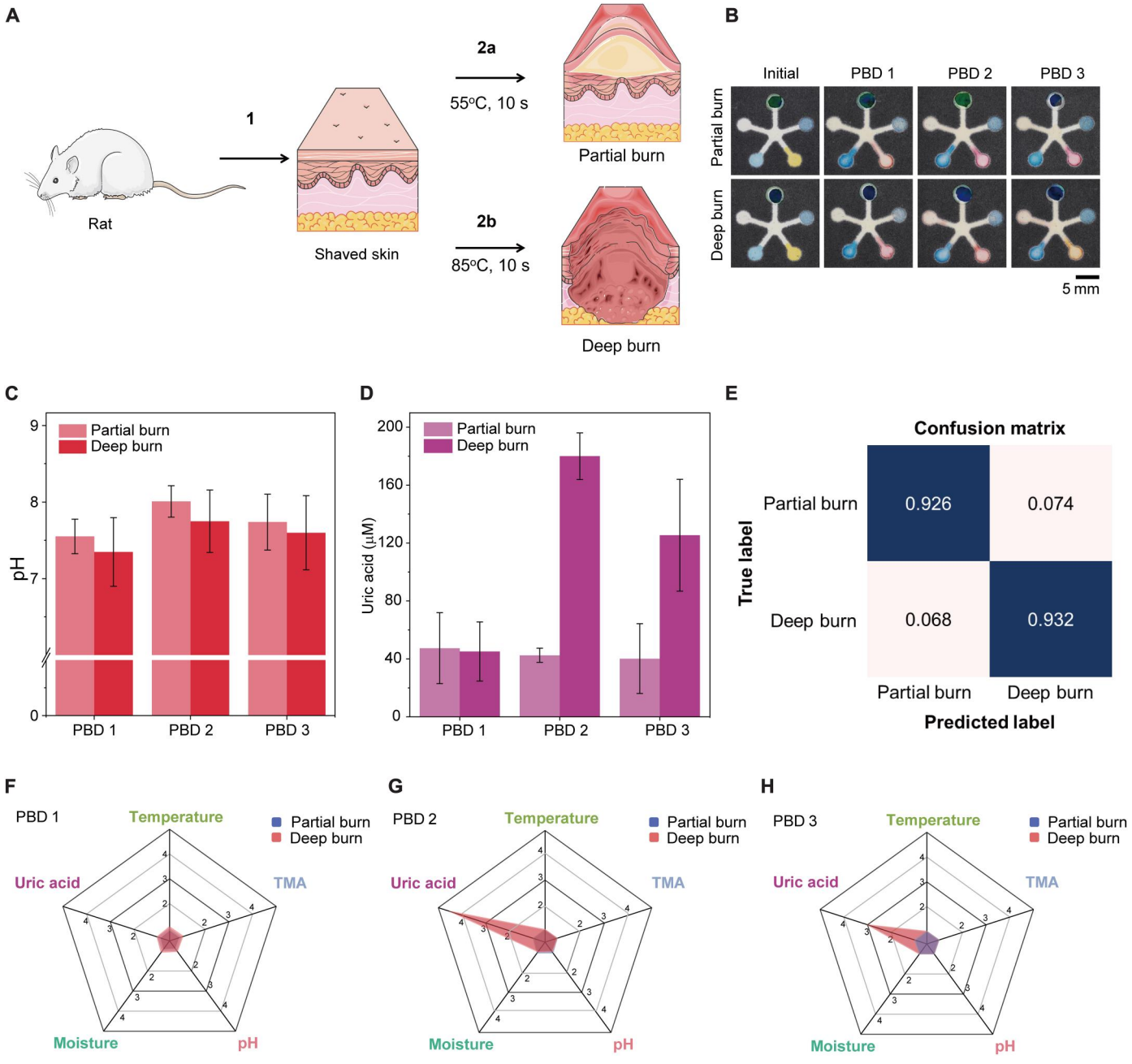

Fig. 5. Ex situ analysis of rat burn wound exudate on benchtop. (**A**) A schematic drawing showing the creation of partial burn versus deep burn. (**B**) Sensor images showing initial colors before burn wound exudate addition and after addition of wound exudate collected from rat partial versus deep burn from 24 hours after burn creation [post-burn day (PBD)] 1 to PBD 3. Quantitative analysis of (**C**) pH trend and (**D**) UA concentration changes over 3 days. Error bars in (C) and (D) represent the SD testing burn wound exudate from three rats. (**E**) Confusion matrix for burn wound severity. (**F** to **H**) The radial graphs for an overview of the five markers on (F) PBD 1, (G) PBD 2, and (H) PBD 3.

at specific time intervals of 1, 3, and 6 hours. The presence of the sensor patches appeared to be well tolerated with no observed signs of discomfort or any excessive scratching of the sensor-covered burn wound.

For the small-sized PETAL sensor patch (1.8 cm size), it requires more than 1 hour to have sufficient wound exudate channeled to the detection zones due to the slow wound exudate generation of 0.34 to 0.43 g/cm^2 per 24 hours (*54*), and the most representative images were taken at around 3-hour time point. The temperatures for both partial thickness and deep burns were around 36°C on day 0 and gradually dropped on PBD 1 and PBD 2 and stabilized on PBD 3 to ~32°C. No temperature differences were observed between partial thickness and deep burns (Fig. 6D).

The trend of temperature change detected with our PETAL sensor patch agreed well with the trend of temperature profiles measured by infrared thermal camera (fig. S20). The pH values for both

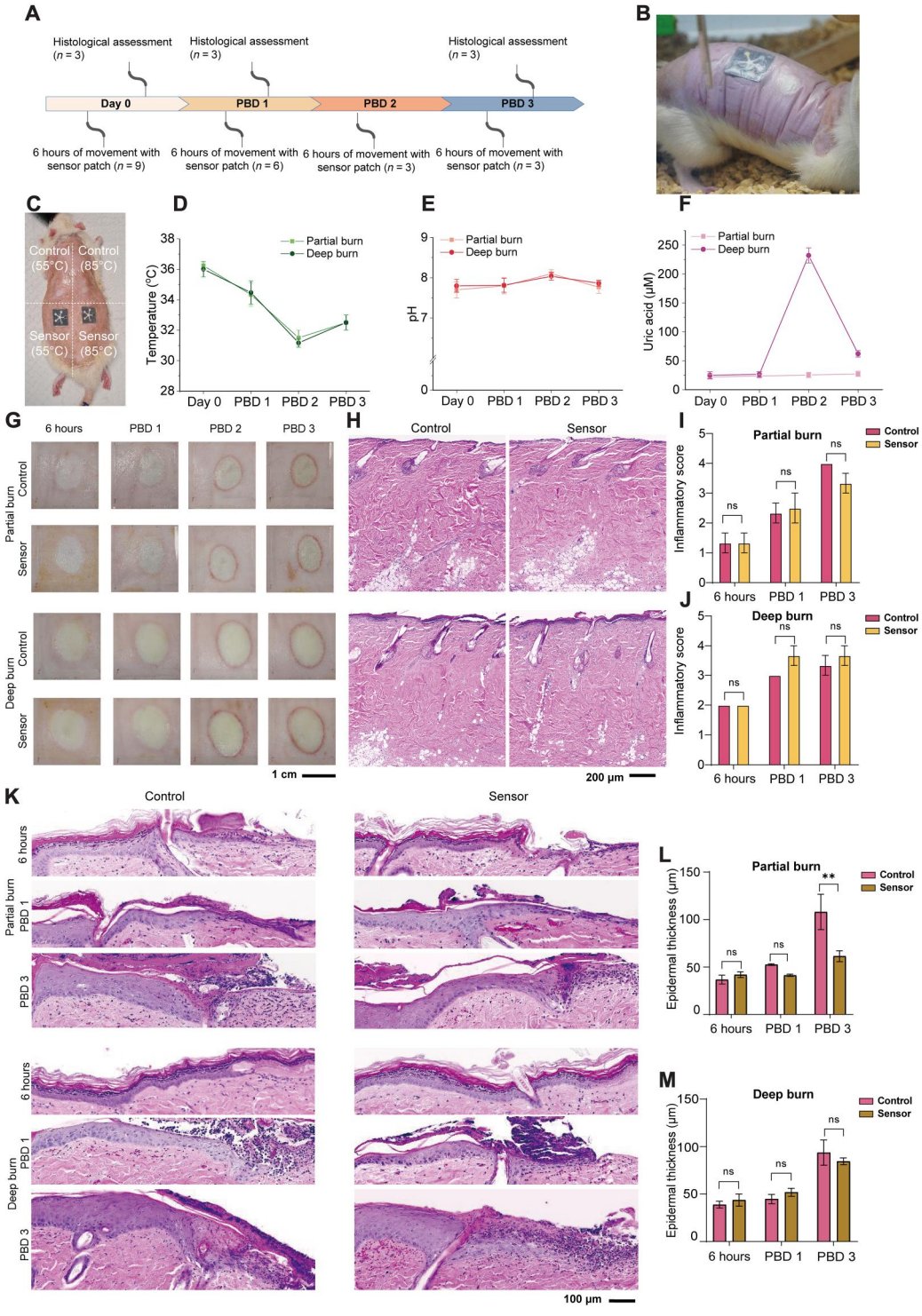

Fig. 6. In situ monitoring of burn wounds and sensor patch biocompatibility in rat burn wound models. (**A**) In situ wound monitoring study design. (**B**) Photograph showing the sensor patches worn on a freely moving rat. (**C**) Photograph showing the burn wounds and the experimental arrangement of the sensor patch attachment, i.e., the sensor patches are placed at the bottom row, whereas the top two burn wounds are used as controls. Quantitative comparison of (**D**) temperature, (**E**) pH, and (**F**) UA for the partial burns versus the deep burns. (**G**) Macroscopic images of the burn wounds from day 0 to PBD 3. (**H**) Hematoxylin and eosin (H&E) images of the burn wounds without sensor (control) versus with sensor on PBD 1. The statistical comparison of inflammatory scores for (**I**) partial burn and (**J**) deep burn for day 0, PBD 1, and PBD 3. (**K**) H&E images showing the wound edge epithelial region for control versus sensor attached burn wound. The statistical comparison of epithelial thickness for (**L**) partial burn and (**M**) deep burn for day 0, PBD 1, and PBD 3. Data are presented as mean values ± SEM. Statistical comparisons were made using two-way analysis of variance (ANOVA) with post hoc Sidak's test (**$P < 0.01$, $n = 3$). ns, not significant.

partial thickness burns and deep burns were all in alkaline range similarly from day 0 to PBD 3 but increased from around 7.8 on day 0 to 8.2 on PBD 2 and then dropped back to 7.8 on PBD 3 (Fig. 6E). The UA levels for the partial thickness and deep burns were both low (~30 μM) on day 0 and PBD 1.

The average UA level for the deep burns increased more than fivefold to 220 μM on PBD 2, whereas it remained at 30 μM in the partial thickness burns (Fig. 6F). On PBD 3, the level for the deep burns reduced substantially to 70 μM but was still higher than that in the partial burns. This higher UA level detected in deep burns in situ agreed with the UA trend observed in the precollected burn wound exudates tested on bench top, similarly showing a higher UA level for deep burns on PBD 2 and PBD 3. This trend also agreed well with literature reports that elevation of serum UA level is correlated with burn wound severity (*38*, *39*).

To study the biocompatibility of our PETAL sensor patch, further characterizations of the burn wounds were performed (Fig. 6, G to M). The macroscopic images of the wounds and the hematoxylin and eosin (H&E)–stained sections show that there are no visible changes in the appearance of the wounds with and without PETAL sensor patches (Fig. 6, G and H). If comparing between the deep and partial thickness burn wounds, the former appears larger than latter. Furthermore, the deep burn wounds appear more blanched compared to the partial burns. The red ring of inflammation as observed on PBD 2 and PDB 3 is consistent around the wounds of both the partial thickness burn and deep burn (Fig. 6G). The histology of PBD 1 wounds shows damage to the hair follicles and coagulated dermis and presence of leukocytes in the tissue is consistent in the sensor-free control and sensor patch attached wounds of partial thickness burns and deep burns (Fig. 6H).

In addition, histological examination of the burn wounds demonstrates significant morphological differences between the partial thickness and deep burns, especially in terms of the existence of hyperthickened epidermis in deep burns (Fig. 6K). There was no significant difference observed in the partial thickness burn wound edge epidermal thickness at 6 hours and PBD 1. At PBD 3, there was a significant difference in epidermal thickness between control (no sensor covering) and sensor-covered wounds. The presence of a sensor patch could have assisted as a skin barrier protection to advance keratinocyte migration and reduce epidermal thickness over the burn wound bed (Fig. 6L). No significant differences were observed in the wound edge epidermal thickness in deep burn control and sensor patch covered wounds (Fig. 6M). These results and observations together suggest that there are no apparent signs of adverse reactions observed on the skin surface in contact with the PETAL sensor patches over 4 days (Fig. 6, G to M). The behavioral, visual, and histological data presented in this section proved the biocompatibility and usability of our PETAL sensor for in situ wound monitoring.

DISCUSSION

We report a PETAL sensor patch that allows simultaneous sensing of five wound markers and/or wound condition indicators using adaptable wax printing sensor layout, intricate sensor functionalization techniques, and a deep neural network–based image analysis algorithm. We have demonstrated the promising outcome of the PETAL sensor platform for bench top analysis of perturbed wound exudate and detection of wound healing of burn wounds both on bench top (ex situ) and in animal models (in situ).

The five markers/parameters are temperature, TMA, pH, moisture, and UA, which together give a holistic profiling of wound infection and inflammation status within minutes of sufficient exudate accumulation. Such holistic collection of five markers/parameters of different clinical implications, i.e., inflammation, infection, and wound physical conditions, is demonstrated using a panel of colorimetric sensors. The biocompatible PETAL sensor can perform in situ multiplexed wound sensing, making it possible for its integration into active wound dressing in future.

Manual interpretation of image values from multiple markers is not practical as a time-efficient wound care routine and real-time monitoring. To enhance the usability of PETAL for on-site assessment, we thus directly analyzed the images or videos of the PETAL sensor patches by deep learning neural networks, which enable a highly accurate wound classification (in our case, identifying delayed healing and burn severity). Such classifications can provide an early warning for adverse events, such as infection or prolonged inflammation, to trigger timely clinical intervention.

We foresee two limitations for our PETAL sensor patch: (i) because the sensor is paper-based and mainly relies on passive capillary action (without active pumping) to draw wound exudates to its detection zones, when the exudate production rate is low or when the exudate is extremely viscous, a longer time is needed (up to hours) to accumulate sufficient exudate on the sensor patches to generate color response. However, because wound healing is a multiple-stage event, usually taking days or weeks (*22*), wound exudate accumulation within hours is still practical. If one needs to get the readout faster, then the pattern design can be optimized, e.g., reducing the channel length. (ii) We have added a blood filtration layer to prevent the red blood cells from interfering with colorimetric readout, which should be applicable to most types of wound exudates, such as serous or serosanguineous exudate (*55*–*57*). However, in case of high blood containing wound exudate (i.e., sanguineous wound), the interference may still exist. In such incident, additional blood filtration via a thicker filtration layer or higher filtration capacity layer (*58*) may be applied. Meanwhile additional augmentation in algorithm (e.g., hue/saturation jitter) can be implemented to ensure the sensor accuracy. In addition to wound classification with the current algorithm, further development of the algorithm could combine regression and classification in the CNN to produce multiple outputs for wound labels and individual marker values. Training with more data from wound models could further enhance the algorithm′s performance and enable rapid quantification of individual markers, which is valuable for quantitative assessment of internal status of the wound.

As for the cost, our PETAL sensor is definitely a cost-effective solution. Not to mention the fact of five makers being detected in one patch, the infection detection itself via the metabolite (e.g., TMA in this example) eliminated the need for costly bacteria culture process. With a proper selection of various bacteria VOCs, our sensor can offer fast identification of bacterial infection.

Note that the AI-enabled PETAL technology can be adaptable and customizable for other wound types, by incorporation of different colorimetric sensors, for example, glucose, lactate, or interleukin-6 for diabetic ulcers. The sensor patch is easily reconfigured for different numbers of detection zones to detect desired number of

biomarkers at the same time so as to broaden its applications for different wound types.

MATERIALS AND METHODS

Chemicals and materials

Glucose, UA, TMA, HRP, uricase, phenol red, 3,3′,5,5′-tetramethylbenzidine, 4-AAP, Stabilicoat Immunoassay Stabilizer solution, sodium 3,5-dichloro-2-hydroxybenzenesulfonate (DHBS), cobalt chloride, PVA, perfluorooctyl-trimethoxysilane, Reichardt's dye, COC, CB, and CN were obtained from Merck. LF1, MF1 grade blood filtration membranes, and grade 3 filter papers were purchased from Whatman.

Wax printing of paper fluidic patterns

The desired two-dimensional (2D) paper fluidic pattern was first drawn using a computer-aided design software with varied dimensions of 1.8-, 2.5-, and 3.5-cm squares and varied size of the sensing regions and channel width to suit different wound size and level of wound fluid (fig. S2). Next, the 2D patterns were printed onto grade 3 Whatman filter paper using a wax printer (Xerox ColorQube 8580 Color Printer) similar to previous reports (*26*–*28*). The wax-printed paper was then heated at 90°C for 10 min to ensure sufficient penetration of wax barriers into the filter paper and, at the same time, to maintain smooth fluid flow in the channels.

PETAL colorimetric sensor development and calibration

According to the sensing materials involved, the five colorimetric sensors in the petal arrangement were prepared at the five detection zones in a sequence of TMA sensor (zone 2), temperature sensor (zone 1), pH sensor (zone 3), moisture sensor (zone 4), and UA sensor (zone 5) (Fig. 2A), and details of preparing each sensor are described in the same order below.

The TMA sensor was prepared by first treating the cellulose paper with 1% perfluorooctyl-trimethoxysilane at 90°C, followed by the deposition of Reichardt's dye (5 mg/ml in ethanol). It was calibrated by adding increasing concentrations of TMA in the wound relevant range of 0 to 300 ppm and incubated for 30 min. Temperature sensor made of CLC mixture containing 36% COC, 10% CB, and 54% CN was sandwiched between two pieces of transparent films with a black background. This sandwiched temperature sensor was then adhered onto the first detection zone of the wax-printed sensor panel. The temperature sensor was calibrated on a high-precision hot plate (Thermo Scientific RT2 Advanced Hotplate Stirrer with 0.1°C resolution) with temperature tuned from 31° to 36°C. A thermal camera (Fluke Ti480 PRO Infrared Camera) was used to confirm the temperature measured by sensor patch. The temperature sensor was placed at the exact same spot during calibration to ensure temperature consistency.

The pH sensor was fabricated by dropping 1 μl of phenol red solution (0.04 wt % in H_2O) twice onto the detection zone. pH calibration was performed by adding 5 μl of standard pH buffers prepared according to a reported protocol (*59*). The actual pH was also verified using a pH meter (HORIBA compact pH meter). The moisture sensor was fabricated by drop-casting 2 μl of $CoCl_2$ (100 mg/ml) dissolved in 2 wt % PVA solution into the fourth detection zone. It was calibrated in a humidity chamber with an inbuilt electronic humidity sensor (Espec, SH-262) with the moisture level adjusted from 30 to 80%.

In the last detection zone, the colorimetric UA sensor was based on a well-developed enzyme cascade reaction (*43*), which requires five steps: (i) addition of 1 wt % low–molecular weight chitosan at pH 6.5 as sensor matrix and dry at room temperature for 5 min; (ii) addition of 16 mM 4-AAP in 8 mM DHBS and dry for 5 min; (iii) addition of HRP (0.15 mg/ml) in a StabilCoat Immunoassay Stabilizer solution and dry for 5 min; (iv) addition of uricase (40 mg/ml) in stabilizer solution and dry for 5 min; and (v) readdition of AAP solution and dry for 5 min. The sequence of these steps has been optimized to make sure that the color gradient is most prominent. The volume of the solution is depending on the area of the well, approximately 14 μl/cm^2. UA sensor was calibrated by adding prepared UA solutions to the sensor and incubating for 15 min. Calibration experiments were performed in triplicates.

Assembly of silicone-embedded PETAL sensor patch

The top transparent layer is a 3M Tegaderm Transparent Film, and the bottom adhesive layer is a Mepitel gentle two-sided wound contact layer if the sensor will be in direct contact with wound. The top Tegaderm layer, wax-printed sensor patch, circular blood filtration membrane (Whatman LF1 grade, 6 mm in diameter), and the bottom adhesive layer were stacked in order and then assembled by sticking together with the sides trimmed to form a complete sensor patch. 3M 2477P medical silicone tape can also be used as the bottom adhesive layer.

Preparation of SWFs

SWF was prepared according to a reported formulation (*45*), which consists of 2% human serum albumin, 0.36% NaCl, 0.05% $NaHCO_3$, 0.02% sodium citrate, 0.1% sodium lactate, 0.1% glucose, 0.01% $CaCl_2.2H_2O$, 0.02% $MgCl_2$, and 0.01% urea. The intended analyte target, i.e., UA and TMA, was spiked in this basic formulation to form healthy healing SWF-A containing 600 μM UA and 0-ppm TMA and nonhealing SWF-B containing 60 μM UA and 300-ppm TMA.

Color analysis and PETAL sensor calibration

Images of the colorimetric sensors before SWF addition were captured as the background, with a mobile phone (SAMSUNG Galaxy Note 20) under a room light condition. JPEG images were used instead of RAW images, considering that JPEG is the most common and user-friendly file format for digital image acquisition devices, but RAW requires extensive tuning of processing parameters. Otherwise, the image quality is deteriorated (fig. S21). Images were captured under ambient light sources with color temperatures ranging from 4000 to 7500 K with auto white balance function ON in the mobile device. Under such conditions, the color features are consistent (or all within a reasonable range) (fig. S22).

After the color change stabilizes at typically 15 min upon analyte addition, images of the sensor patches (regardless of the wet/dry state) were captured again. The timing is set at 15 min to ensure that the sensor patch is fully reacted, so that they will give similar readings regardless of wet or dry condition at four nodes (except moisture) using the analysis method used for sensor calibration (fig. S23). There are slight shifts across feature values due to the different image sensors and image signal processor algorithms applied in different mobile devices (fig. S24). The images were then analyzed by ImageJ software to obtain the intensity or RGB values of the detection zones. These intensity values or RGB values were then

background-subtracted and compared with calibration values to determine the corresponding analyte concentrations. Temperature sensor reflectance value from the image was analyzed by AttoView software (Attonics).

Collection of rat wound exudate and PETAL sensor patch testing

A perturbed wound model in rats was induced by first placing an oversized electrospun scaffold made of polycaprolactone with 20% collagen type 1, presoaked in senescence-inducing drug, FK866, into a full-thickness 6-mm wound on the back of male Sprague-Dawley rats (6 to 8 weeks old, 250 to 300 g). These scaffolds were left in situ for 10 days before scaffold removal. Perturbed wounds were observed to have features mimicking human chronic wounds such as stalled reepithelization with hyperthickening at the wound edge and hindered wound closure and chronic inflammation (*49*). The animal procedures for perturbed wound were performed under protocol number A19055, approved by the Institutional Animal Care and Use Committee (IACUC) of Nanyang Technological University. Exudates from the perturbed wounds were collected upon the removal of the scaffolds. For rat perturbed wound model, the wound fluid amount is low; therefore, we pooled wound fluids from four to six rats together for ex situ measurements. To elute the wound exudate from the scaffolds removed, scaffolds were first cut into fragments before ribonuclease-free distilled water was added, vortex for 2 min at maximum speed, and then centrifuged at 5000*g* for 5 min to obtain the scaffold-eluted fluids. The perturbed wound exudate was further ultrafiltered at 3000 rpm for 10 min before it was added to the sensor patch. The images of the sensor patch before and after 15 min of exudate addition were captured for color analysis.

Two types of burns were created on the shaved back of rats at 55° and 85°C for 10 s, respectively. A handheld soldering iron was used to create consistent burns. The burn wounds were then gently debrided with gauze and bandaged with Tegaderm and Opsite for wound fluid collection. The burn wound fluids from three rats (>100 μl from the four 6-mm burns per rat overnight) were collected by pipetting the exudate accumulated under Tegaderm into sampling tubes on PBD 1 to PBD 3. The burn wound exudate was directly added onto the center port of the PETAL sensor patch without any pretreatment. The images of the sensor patch before and after 15 min of exudate addition were taken for color analysis.

Evaluation of PETAL sensor patch in rat burn wound model

Animal procedures

The animal procedures for burn wound model were performed under protocol number A19039, approved by the IACUC of the Animal Research Facility of Nanyang Technological University. Sprague-Dawley male rats aged 6 to 8 weeks old, weighing 200 to 250 g were purchased from InVivos Pte Ltd. (Singapore) and acclimatized before conducting burn experiments. The burn wounds were created and debrided as described above. Both sides of sensor patches were first sterilized by ultraviolet for 20 min to ensure sterility. The sterilized patches were then applied onto the debrided burn wounds and were secured in place with a Tegaderm film and wrapped with Opsite. The rats were then monitored for 6 hours. The rats were euthanized on 6 hours after burn, PBD 1 and PBD 3, to examine the histology of the burn wound.

Tissue processing, microtome sectioning, and H&E staining

Harvested tissues were fixed in 4% paraformaldehyde for 48 hours. Fixed tissues were bisected and processed in a HistoCore PEARL tissue processor (Leica, Germany). Briefly, the samples undergo increasing changes of ethanol and into xylene. Samples were then transferred into a warm bath of paraffin at 65°C and embedded into a paraffin block. The embedded blocks were sectioned at 5 μm using Leica Microtome RM2245 (Leica, Germany) and mounted onto polysine microscope slides. Sectioned slides were baked, and H&E was performed in Leica Autostainer XL (Leica, Germany). Briefly, slides were dewaxed in Clearene and hydrated in decreasing concentrations of ethanol. Slides were then dipped into hematoxylin and washed in water before staining in eosin. Subsequently, the slides were dehydrated in increasing concentrations of ethanol and cleared into Clearene. Slides were cover-slipped using limonene mounting medium (Sigma-Aldrich, USA).

Bright-field microscopy and image analysis

H&E-stained slides were scanned on an Axioscan.Z1 slide scanner (Zeiss, Germany) using 20× objective with numerical aperture of 0.8. Scanned images were visualized on Zen 3.3 software (Zeiss, Germany), and regions of interest (ROIs) were drawn for analysis of epidermal thickness and inflammatory score. For epidermal thickness measurement, the line function was used to draw seven-line ROIs from the thickest spinosus layer to the basal cell layer. The measured ROIs were averaged, and analysis were performed. Two-way analysis of variance (ANOVA) with Sidak's multiple comparisons was performed on GraphPad Prism 8.4.3 to confer statistical significance. A P value of 0.05 was considered statistically significant.

Development of machine learning algorithm

JPEG (standard RGB color space) images of sensors were taken from a mobile phone (SAMSUNG Galaxy Note 20) or a digital camera (Sony A7RIII, Panasonic DC-G9). A total of 1765 images from perturbed wound model and 1193 images from burn wound model were obtained. Images are generally taken 8 to 15 min after fluid addition. During image collection, we also varied the shooting angle and lighting.

After acquiring all sensor images, the rectangular shape of the sensor is extracted and cropped out on the basis of size using MATLAB Image processing toolbox. After cropping, sensor images were resized to 227 × 227, which then denoised with a pretrain denoising neural network (DnCNN) (*60*) to remove excessive noise in certain dark region. Images from the training set are augmented with rotation/pixel translation, shear, and color jitter to mimic the actual use of this framework.

CNN is constructed following Fig. 1E using deep network designer (Deep Learning Toolbox, MATLAB R2021b) (*61*, *62*). Parallel computing toolbox is used to speed up the training process. Because our sample size is small, here, we chose to restrict our network size by only including three convolutional layers and two fully connected layers. An ablation experiment indicates that there is a limited performance enhancement if the convolution layers are further increased and that the performance drops if the convolution layers are reduced (fig. S25). Because there were two separate wound models, the definitions of normal/healable condition were different for pH and UA marker. Two binary image classifiers were trained for two types of wound models (normal versus perturb, and partial thickness burn versus full thickness burn) with the same structure

but different weights. Models were trained on a workstation (AMD Ryzen Threadripper 3990X, NVIDIA GeForce RTX3090) for 100 epochs, with a learning rate of 0.005.

Training accuracy and loss for both models are shown in figs. S16 to S18. Fivefold cross-validation was used to minimize the error of the training process. Twenty percent of images in the dataset was allocated as validation sets.

Traditional regression analysis techniques, such as linear regression (*63*, *64*), were also used to construct our calibration and interpret individual marker levels to understand the classification results. Compared to standard linear regression models, CNN offers fully connected layer architecture, with multiple layers of linear operations and nonlinear activation functions. This architecture allows CNN to learn nonobvious patterns from a large set of variables, making them a powerful tool for multiplexed sensor interpretation and quantification.

Supplementary Materials

This PDF file includes:

Supplementary Text
Figs. S1 to S25
Tables S1 and S2
References

View/request a protocol for this paper from *Bio-protocol*.

REFERENCES AND NOTES

1. J. S. Chin, L. Madden, S. Y. Chew, D. L. Becker, Drug therapies and delivery mechanisms to treat perturbed skin wound healing. *Adv. Drug Deliv. Rev.* **149-150**, 2–18 (2019).
2. Y. Wang, M. Guo, B. He, B. Gao, Intelligent patches for wound management: In situ sensing and treatment. *Anal. Chem.* **93**, 4687–4696 (2021).
3. M. Ruiz-Castilla, O. Roca, J. R. Masclans, J. P. Barret, Recent advances in biomarkers in severe burns. *Shock* **45**, 117–125 (2016).
4. T. R. Dargaville, B. L. Farrugia, J. A. Broadbent, S. Pace, Z. Upton, N. H. Voelcker, Sensors and imaging for wound healing: A review. *Biosens. Bioelectron.* **41**, 30–42 (2013).
5. D. Church, S. Elsayed, O. Reid, B. Winston, R. Lindsay, Burn wound infections. *Clin. Microbiol. Rev.* **19**, 403–434 (2006).
6. A. Mischnik, M. Mieth, C. J. Busch, S. Hofer, S. Zimmermann, First evaluation of automated specimen inoculation for wound swab samples by use of the Previ Isola system compared to manual inoculation in a routine laboratory: Finding a cost-effective and accurate approach. *J. Clin. Microbiol.* **50**, 2732–2736 (2012).
7. D. M. Anisuzzaman, C. Wang, B. Rostami, S. Gopalakrishnan, J. Niezgoda, Z. Yu, Image-based artificial intelligence in wound assessment: A systematic review. *Adv. Wound Care* **11**, 687–709 (2022).
8. D. Lou, Q. Pang, X. Pei, S. Dong, S. Li, W.-q. Tan, L. Ma, Flexible wound healing system for pro-regeneration, temperature monitoring and infection early warning. *Biosens. Bioelectron.* **162**, 112275 (2020).
9. B. Qiao, Q. Pang, P. Yuan, Y. Luo, L. Ma, Smart wound dressing for infection monitoring and NIR-triggered antibacterial treatment. *Biomater. Sci.* **8**, 1649–1657 (2020).
10. P. Kassal, J. Kim, R. Kumar, W. R. de Araujo, I. M. Steinberg, M. D. Steinberg, J. Wang, Smart bandage with wireless connectivity for uric acid biosensing as an indicator of wound status. *Electrochem. Commun.* **56**, 6–10 (2015).
11. Z. Xiong, S. Achavananthadith, S. Lian, L. E. Madden, Z. X. Ong, W. Chua, V. Kalidasan, Z. Li, Z. Liu, P. Singh, H. Yang, S. P. Heussler, S. M. P. Kalaiselvi, M. B. H. Breese, H. Yao, Y. Gao, K. Sanmugam, B. C. K. Tee, P. Y. Chen, W. Loke, C. T. Lim, G. S. H. Chiang, B. Y. Tan, H. Li, D. L. Becker, J. S. Ho, A wireless and battery-free wound infection sensor based on DNA hydrogel. *Sci. Adv.* **7**, eabj1617 (2021).
12. S. Kalasin, P. Sangnuang, W. Surareungchai, Intelligent wearable sensors interconnected with advanced wound dressing bandages for contactless chronic skin monitoring: Artificial intelligence for predicting tissue regeneration. *Anal. Chem.* **94**, 6842–6852 (2022).
13. S. Shrivastava, T. Q. Trung, N.-E. Lee, Recent progress, challenges, and prospects of fully integrated mobile and wearable point-of-care testing systems for self-testing. *Chem. Soc. Rev.* **49**, 1812–1866 (2020).
14. S. Bauer, Sophisticated skin. *Nat. Mater.* **12**, 871–872 (2013).
15. D.-H. Kim, N. Lu, R. Ma, Y.-S. Kim, R.-H. Kim, S. Wang, J. Wu, S. M. Won, H. Tao, A. Islam, K. J. Yu, T.-i. Kim, R. Chowdhury, M. Ying, L. Xu, M. Li, H.-J. Chung, H. Keum, M. McCormick, P. Liu, Y.-W. Zhang, F. G. Omenetto, Y. Huang, T. Coleman, J. A. Rogers, Epidermal electronics. *Science* **333**, 838–843 (2011).
16. J. A. Rogers, T. Someya, Y. Huang, Materials and mechanics for stretchable electronics. *Science* **327**, 1603–1607 (2010).
17. B. C. K. Tee, J. Ouyang, Soft electronically functional polymeric composite materials for a flexible and stretchable digital future. *Adv. Mater.* **30**, 1802560 (2018).
18. Y. Zhao, A. Kim, G. Wan, B. C. K. Tee, Design and applications of stretchable and self-healable conductors for soft electronics. *Nano Converg.* **6**, 25 (2019).
19. T. Djenizian, B. C. K. Tee, M. Ramuz, L. Fang, Advances in flexible and soft electronics. *APL Materials* **7**, 031201 (2019).
20. Q. Pang, D. Lou, S. Li, G. Wang, B. Qiao, S. Dong, L. Ma, C. Gao, Z. Wu, Smart flexible electronics-integrated wound dressing for real-time monitoring and on-demand treatment of infected wounds. *Adv. Sci.* **7**, 1902673 (2020).
21. B. K. Ashley, M. S. Brown, Y. Park, S. Kuan, A. Koh, Skin-inspired, open mesh electrochemical sensors for lactate and oxygen monitoring. *Biosens. Bioelectron.* **132**, 343–351 (2019).
22. C. Wang, E. Shirzaei Sani, W. Gao, Wearable bioelectronics for chronic wound management. *Adv. Funct. Mater.* **32**, 2111022 (2022).
23. P. Mostafalu, A. Tamayol, R. Rahimi, M. Ochoa, A. Khalilpour, G. Kiaee, I. K. Yazdi, S. Bagherifard, M. R. Dokmeci, B. Ziaie, S. R. Sonkusale, A. Khademhosseini, Smart bandage for monitoring and treatment of chronic wounds. *Small* **14**, 1703509 (2018).
24. Y. Gao, D. T. Nguyen, T. Yeo, S. B. Lim, W. X. Tan, L. E. Madden, L. Jin, J. Y. K. Long, F. A. B. Aloweni, Y. J. A. Liew, M. L. L. Tan, S. Y. Ang, S. D. O. Maniya, I. Abdelwahab, K. P. Loh, C.-H. Chen, D. L. Becker, D. Leavesley, J. S. Ho, C. T. Lim, A flexible multiplexed immunosensor for point-of-care in situ wound monitoring. *Sci. Adv.* **7**, eabg9614 (2021).
25. S. RoyChoudhury, Y. Umasankar, J. Jaller, I. Herskovitz, J. Mervis, E. Darwin, P. A. Hirt, L. J. Borda, H. A. Lev-Tov, R. Kirsner, S. Bhansali, Continuous monitoring of wound healing using a wearable enzymatic uric acid biosensor. *J. Electrochem. Soc.* **165**, B3168–B3175 (2018).
26. J. T. Connelly, J. P. Rolland, G. M. Whitesides, "Paper machine" for molecular diagnostics. *Anal. Chem.* **87**, 7595–7601 (2015).
27. M. S. Verma, M. N. Tsaloglou, T. Sisley, D. Christodouleas, A. Chen, J. Milette, G. M. Whitesides, Sliding-strip microfluidic device enables ELISA on paper. *Biosens. Bioelectron.* **99**, 77–84 (2018).
28. E. Carrilho, A. W. Martinez, G. M. Whitesides, Understanding wax printing: A simple micropatterning process for paper-based microfluidics. *Anal. Chem.* **81**, 7091–7095 (2009).
29. Y. Zhu, J. Zhang, J. Song, J. Yang, Z. Du, W. Zhao, H. Guo, C. Wen, Q. Li, X. Sui, L. Zhang, A multifunctional pro-healing zwitterionic hydrogel for simultaneous optical monitoring of pH and glucose in diabetic wound treatment. *Adv. Funct. Mater.* **30**, 1905493 (2020).
30. M. S. Brown, B. Ashley, A. Koh, Wearable technology for chronic wound monitoring: Current dressings, advancements, and future prospects. *Front. Bioeng. Biotechnol.* **6**, 47 (2018).
31. V. Dini, P. Salvo, A. Janowska, F. D. Francesco, A. Barbini, M. Romanelli, Correlation between wound temperature obtained with an infrared camera and clinical wound bed score in venous leg ulcers. *Wounds* **27**, 274–278 (2015).
32. J. Bayuo, Management strategies of burns associated hyperthermia: A case report. *Burns Open* **1**, 45–47 (2017).
33. S. Ono, R. Imai, Y. Ida, D. Shibata, T. Komiya, H. Matsumura, Increased wound pH as an indicator of local wound infection in second degree burns. *Burns* **41**, 820–824 (2015).
34. E. Osti, Skin ph variations from the acute phase to re-epithelialization in burn patients treated with new materials (burnshield, semipermeable adhesive film, dermasilk, and hyalomatrix). Non-invasive preliminary experimental clinical trial. *Ann. Burns Fire Disasters* **21**, 73–77 (2008).
35. M. Ochoa, R. Rahimi, B. Ziaie, Flexible sensors for chronic wound management. *IEEE Rev. Biomed. Eng.* **7**, 73–86 (2014).
36. L. D. J. Bos, P. J. Sterk, M. J. Schultz, Volatile metabolites of pathogens: A systematic review. *PLOS Pathog.* **9**, e1003311 (2013).
37. C. Salinas Alvarez, D. Sierra-Sosa, B. Garcia-Zapirain, D. Yoder-Himes, A. Elmaghraby, A detection of volatile compounds emitted by bacteria in wounds using gas sensors. *Sensors* **19**, 1523 (2019).
38. M. L. Fernandez, Z. Upton, H. Edwards, K. Finlayson, G. K. Shooter, Elevated uric acid correlates with wound severity. *Int. Wound J.* **9**, 139–149 (2012).
39. J. Liang, P. Zhang, X. Hu, L. Zhi, Elevated serum uric acid after injury correlates with the early acute kidney in severe burns. *Burns* **41**, 1724–1731 (2015).
40. C. Reichardt, Solvatochromic dyes as solvent polarity indicators. *Chem. Rev.* **94**, 2319–2358 (1994).

41. J. B. Essner, G. A. Baker, Ionic liquid inspired alkalinochromic salts based on Reichardt's dyes for the solution phase and vapochromic detection of amines. *Anal. Bioanal. Chem.* **410**, 4607–4613 (2018).
42. A. Koh, D. Kang, Y. Xue, S. Lee, R. M. Pielak, J. Kim, T. Hwang, S. Min, A. Banks, P. Bastien, M. C. Manco, L. Wang, K. R. Ammann, K.-I. Jang, P. Won, S. Han, R. Ghaffari, U. Paik, M. J. Slepian, G. Balooch, Y. Huang, J. A. Rogers, A soft, wearable microfluidic device for the capture, storage, and colorimetric sensing of sweat. *Sci. Transl. Med.* **8**, 366ra165 (2016).
43. X. Wang, F. Li, Z. Cai, K. Liu, J. Li, B. Zhang, J. He, Sensitive colorimetric assay for uric acid and glucose detection based on multilayer-modified paper with smartphone as signal readout. *Anal. Bioanal. Chem.* **410**, 2647–2655 (2018).
44. Y. Yang, E. Noviana, M. P. Nguyen, B. J. Geiss, D. S. Dandy, C. S. Henry, Paper-based microfluidic devices: Emerging themes and applications. *Anal. Chem.* **89**, 71–91 (2017).
45. C. Öhlknecht, G. Tegl, B. Beer, C. Sygmund, R. Ludwig, G. M. Guebitz, Cellobiose dehydrogenase and chitosan-based lysozyme responsive materials for antimicrobial wound treatment. *Biotechnol. Bioeng.* **114**, 416–422 (2017).
46. N. J. Trengove, S. R. Langton, M. C. Stacey, Biochemical analysis of wound fluid from nonhealing and healing chronic leg ulcers. *Wound Repair Regen.* **4**, 234–239 (1996).
47. R. Ghosh, V. Vaishampayan, A. Mahapatra, R. Malhotra, S. Balasubramanian, A. Kapoor, Enhancement of limit of detection by inducing coffee-ring effect in water quality monitoring microfluidic paper-based devices. *Desalin. Water Treat.* **156**, 316–322 (2019).
48. K. N. Al-Milaji, H. Zhao, New perspective of mitigating the coffee-ring effect: Interfacial assembly. *J. Phys. Chem. C* **123**, 12029–12041 (2019).
49. J. S. Chin, D. L. Becker, *World Union of Wound Healing Societies Congress*, Abu Dhabi, UAE, 1 to 5 March 2022.
50. R. M. Johnson, R. Richard, Partial-thickness burns: Identification and management. *Adv. Skin Wound Care* **16**, 178–187 (2003).
51. V. Singh, L. Devgan, S. Bhat, S. M. Milner, The pathogenesis of burn wound conversion. *Ann. Plast. Surg.* **59**, 109–115 (2007).
52. A. J. Singer, S. T. Boyce, Burn wound healing and tissue engineering. *J. Burn Care Res.* **38**, e605–e613 (2017).
53. D. M. Jackson, The diagnosis of the depth of burning. *Br. J. Surg.* **40**, 588–596 (1953).
54. L. O. Lamke, G. E. Nilsson, H. L. Reithner, The evaporative water loss from burns and the water-vapour permeability of grafts and artificial membranes used in the treatment of burns. *Burns* **3**, 159–165 (1977).
55. K. F. Cutting, R. J. White, Maceration of the skin and wound bed. 1: Its nature and causes. *J. Wound Care* **11**, 275–278 (2002).
56. B. Bates-Jensen, G. Schultz, L. G. Ovington, Management of exudate, biofilms, and infection, in *Wound Care: A Collaborative Practice Manual* (Wolters Kluwer, ed. 4, 2012), pp. 457–476.
57. P. Vowden, E. Bond, F. Meuleneire, Managing high viscosity exudate. *Wounds UK* **11**, 56–60 (2015).
58. W. Guo, J. Hansson, W. van der Wijngaart, Synthetic paper separates plasma from whole blood with low protein loss. *Anal. Chem.* **92**, 6194–6199 (2020).
59. R. A. Robinson, R. H. Stokes, *Electrolyte Solutions* (Butterworths, ed. 2, 1968).
60. K. Zhang, W. Zuo, Y. Chen, D. Meng, L. Zhang, Beyond a gaussian denoiser: Residual learning of deep cnn for image denoising. *IEEE Trans. Image Process.* **26**, 3142–3155 (2017).
61. K. Team, Simple MNIST convnet (2022); https://keras.io/examples/vision/mnist_convnet/.
62. L. Guo, T. Wang, Z. Wu, J. Wang, M. Wang, Z. Cui, S. Ji, J. Cai, C. Xu, X. Chen, Portable food-freshness prediction platform based on colorimetric barcode combinatorics and deep convolutional neural networks. *Adv. Mater.* **32**, 2004805 (2020).
63. Z. Lu, N. Lu, Y. Xiao, Y. Zhang, Z. Tang, M. Zhang, Metal-nanoparticle-supported nanozyme-based colorimetric sensor array for precise identification of proteins and oral bacteria. *ACS Appl. Mater. Interfaces* **14**, 11156–11166 (2022).
64. Z. Li, J. R. Askim, K. S. Suslick, The optoelectronic nose: Colorimetric and fluorometric sensor arrays. *Chem. Rev.* **119**, 231–292 (2019).
65. M. T. Ribeiro, S. Singh, C. Guestrin, "Why should I trust you?" Explaining the predictions of any classifier, in *Proceedings of the 22nd ACM SIGKDD International Conference on Knowledge Discovery and Data Mining* (Association for Computing Machinery, 2016), pp. 1135–1144.

Acknowledgments: This work was supported by the Agency of Science Technology and Research (A*STAR). **Funding:** X.T.Z., Z.Y., L.S., Y.Y., N.A.B.M.S., Z.X., X.J.L., B.C.K.T., and X.S. acknowledge Additive Manufacturing of Biological Materials (AMBM) program (A18A8b0059). B.C.K.T. acknowledges support from the National Research Foundation (NRF), Prime Minister's office, Singapore, under its NRF Fellowship (NRFF-2017-08) and iHealthtech grant. M.T., J.S.C., and D.L.B. acknowledge Industry Alignment Fund–Pre-Positioning Programme (IAF-PP) grant number H17/01/a0/0C9 as part of the Wound Care Innovation for the Tropics (WCIT) Programme, IAF-PP grant number H1701a0004, and The Skin Research Institute of Singapore, Phase 2: SRIS@Novena. Z.Y. acknowledges support from NUS Research Scholarship. **Author contributions:** X.T.Z., L.S., N.A.B.M.S., Y.Y., X.J.L., X.S. and B.C.K.T. conceptualized and developed the PETAL sensor system; X.T.Z., L.S., N.A.B.M.S., and Y.Y. performed calibrations, conducted all benchtop experiments, performed image analysis, and prepared sensors for animal experiments; Z.Y. developed the machine learning algorithms and participated in sensor experiments for image capture; Z.Y. and Z.X. contributed to schematic illustrations and discussion; M.T., J.S.C., and D.L.B. contributed to animal model design, provided animal wound exudates, and performed animal experiments; X.T.Z. and Z.Y. drafted the manuscript; D.L.B., B.C.K.T., and X.S. revised the manuscript. **Competing interests:** X.T.Z., L.S., Y.Y., and X.S. are the coinventors of the patent application related to current work. The name of the organization issuing the patent is Intellectual Property Office of Singapore (IPOS). The patent, i.e., Singapore patent application no. SG10202107044R with a priority date of 28 June 2021, has also completed a secondary filing as a PCT patent (PCT/SG2022/050439) to the International Bureau of WIPO (IB) on 27 June 2022. The authors declare that they have no other competing interests. **Data and materials availability:** All data needed to evaluate the conclusions in the paper are present in the paper and/or the Supplementary Materials. Relevant source code can be acquired from 10.5281/zenodo.7783585.

Submitted 18 January 2023
Accepted 11 May 2023
Published 16 June 2023
10.1126/sciadv.adg6670